Aust. J. Phys., 1986, **39**, 271–91

Ionization Growth between Hyperboloidal Needle and Plane Electrode under r.f. Electric Fields in N_2. I Image Intensifier Observations and the Influence of Space Charge Accumulations

N. Sato[A,B] *and S. C. Haydon*[A]

[A] Department of Physics, The University of New England, Armidale, N.S.W. 2351.
[B] Present address: Department of Electrical Engineering, Faculty of Engineering, Hokkaido University, Sapporo 060, Japan.

Abstract

The corona onset and subsequent plasma growth in the space between a hyperboloidal needle and plane electrode is investigated by highly time-resolved image intensifier techniques. The use of the special geometry has enabled appropriate mathematical analysis of space charge effects to be carried out and has provided clarification of the underlying causes of some significant features of ionization growth under r.f. conditions. The effect of u.v. filtering on the corona images is also examined.

1. Introduction

Investigations of the radio frequency discharge have been developed intensively in this laboratory (Plumb *et al.* 1984; Cook and Haydon 1984). Recently, by using a highly sensitive image intensifier system and an optical multi-channel analyser, ns time-resolved observations of the r.f. corona (Sato and Haydon 1984*a*) and spatially resolved spectroscopy (Sato and Haydon 1984*b*) have been carried out with a toroid-to-plane electrode configuration. These have revealed some characteristics of the r.f. discharge such as the polarity effect, hysteresis and the processes associated with space charge redistribution.

The toroid-to-plane electrode configuration was originally investigated because of its relevance to the practical problems arising with HV, highpower transmitting aerials (Dossing *et al.* 1978; Haydon and Plumb 1978). Unfortunately, however, such a configuration is too complex to investigate mathematically. Consequently, for the present study a hyperboloidal needle-to-plane gap configuration is used and a computer simulation is developed for comparison of experimental data with theory. In this way, data on the space charge field variations, calculated by the use of a one-dimensional model in a spheroidal coordinate system, can be compared with the distinctive features of the variations of the corona images. These corona images are observed in the pressure range from 80 to 650 Torr (1 Torr = 133 Pa) and consist of 10 ns snapshots at different phase positions of a single r.f. cycle. They are sampled at various time intervals T after the start of the r.f. pulse, and for a variety of peak applied voltages, by using three stages of image intensification.

0004-9506/86/020271$02.00

For investigations of the intensity variation of the corona image in the gap space, more clearly focused images are obtained with only two multi-channel plate (MCP) intensifiers and the required quantitative data are then obtained with an optical multi-channel analyser system. The effect of a u.v. filter on the appearance of the corona image is also examined.

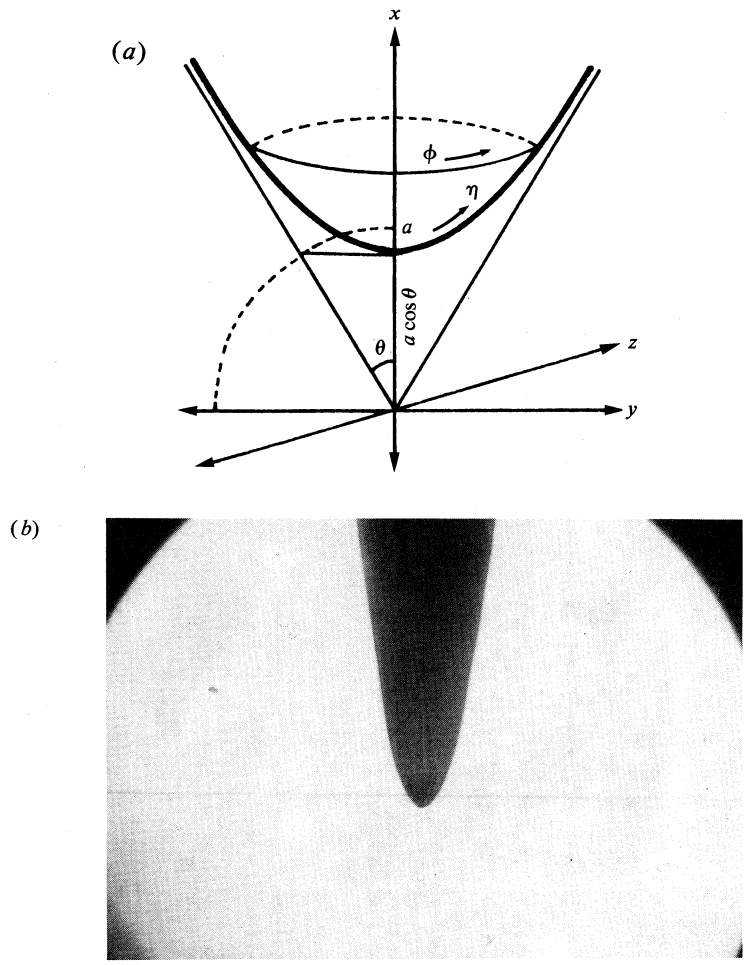

Fig. 1. (*a*) Representation of the hyperboloidal needle-to-plane electrode configuration in spheroidal coordinates. (*b*) Photo-micrograph of the needle electrode taken with a microscope at 60× magnification.

2. Experimental Arrangement and Procedure

The experimental arrangement was basically identical to that described elsewhere (Sato and Haydon 1984*a*). The hyperboloidal needle-to-plane gap configuration used is shown in Fig. 1*a*. The needle electrode of length 25 mm was made of stainless steel, as nearly as possible in the form of a hyperboloid of revolution. The photo-micrograph of the needle, magnified 60 times, is shown in Fig. 1*b*.

The configuration of the electrodes is represented by the spheroidal coordinates (η, θ, ϕ) which are related to the cartesian coordinates (x, y, z) by the transformation equations

$$x = a\cosh\eta\cos\theta, \tag{1}$$

$$y = a\sinh\eta\sin\theta\cos\phi, \tag{2}$$

$$z = a\sinh\eta\sin\theta\sin\phi. \tag{3}$$

For constant $\theta = \theta_0$ and by eliminating both η and ϕ the transformation equations reduce to

$$\frac{x^2}{a^2\cos^2\theta_0} - \frac{y^2+z^2}{a^2\sin^2\theta_0} = 1, \tag{4}$$

which is the standard equation for a hyperbola. The needle and plane electrode surfaces correspond respectively to the surfaces with $\theta = \theta_0$ and $\theta = 90°$ in this equation. The parameter a is related to the tip radius r_0 and needle-to-plane spacing d, where $r_0 = (a^2/d) - d$ and $d = a\cos\theta_0$. The experiments were carried out for pressures from 80 to 650 Torr with a gap length of $d = 12$ mm and a tip radius of $r_0 = 50$ μm. A pulsed r.f. potential of frequency 10 MHz, pulse duration 10 μs, rise time 2 μs and repetition rate 60 Hz was applied to the plane electrode.

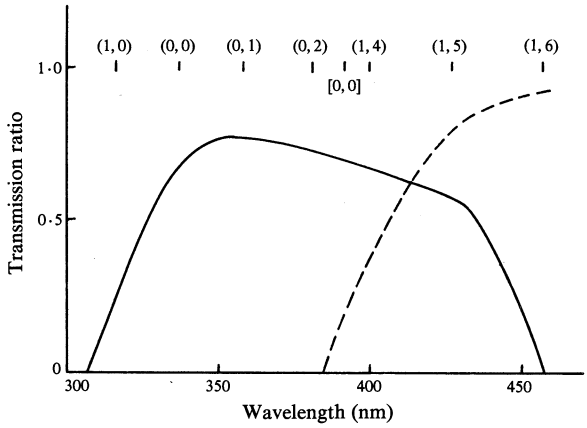

Fig. 2. Combined transmission characteristics of the objective lens and the Kodak filters No. 39 (solid curve) and No. 2C (dashed curve); (v', v'') second positive band; $[v', v'']$ first negative band.

Some changes were made to the previous experimental arrangements to improve the quality of the focused images:

(1) A u.v. bandpass filter (Kodak No. 39) was used to eliminate the colour aberration of the quartz objective lens. The measured bandpass characteristics of the combined filter and quartz lens are shown in Fig. 2, demonstrating that the main spectral lines of the second positive system of the N_2 molecule are transmitted.

(2) Where possible the third-stage magnetic focused image intensifier (MII), which caused a deterioration in the image quality, was eliminated. Applications of the remaining two-stage system are discussed in Section 3*d*.

Snapshots (10 ns duration) of the intensified corona images were observed at specified phase positions within one cycle of the applied r.f. voltage. For comparison, good resolution photographs were obtained with only two stages of MCP intensification and multiple exposures.

Observations of the corona image were made at the rising, middle (plateau) and late part of the r.f. voltage pulse for various values of the r.f. peak voltage. In this way the effect of the applied peak voltage on the variation of the corona image during the r.f. pulse could be examined.

A u.v. filter (Kodak 2C) was used to check the spectroscopic characteristics of the corona image. The measured transmission characteristics of this combination of filter and objective lens (see Fig. 2) indicate that the high intensity emission lines of the second positive system of N_2 are eliminated by this filter.

A quantitative display of the intensity variation in the gap was obtained by viewing the output from the two-stage MCP intensification with an optical multi-channel analyser (OMA2 system).

3. Experimental Results and Discussion

(a) Observation of the Corona Onset

In order to record the very low light levels at the onset of corona, these were observed at the rising part of the r.f. voltage pulse by using the three-stage intensifier system. Fig. 3*a* (i) shows photographs at the corona onset voltage at pressures of 80, 200 and 650 Torr. The luminosity of the discharge became *suddenly* apparent at a *negative* peak voltage of the needle electrode and the axial length of the corona discharge region decreased with increasing pressure.

At the positive peak voltage just prior to this sudden event, luminosities of low intensity could be observed around the needle electrode, as shown in Fig. 3*a* (ii). This luminosity is believed to arise from a *pre-breakdown* excitation process and not from a self-sustained '*breakdown*' of the small volume because the intensity of this luminosity is $\sim\frac{1}{20}$ that of succeeding corona images.

The corona onset voltage V_c measured in the pressure range from 80 to 650 Torr is shown in Fig. 3*b* together with the intermittent breakdown voltage V_i and continuous spark breakdown voltage V_{sc}. The axial length of the corona discharge region d_c at corona onset voltage was measured from the image recorded by the image intensifier system. The corresponding curve of V_c against pd_c (broken curve in Fig. 3*b*) agrees with the extrapolation of the V_{sc} against pd curve, indicating that the corona discharges observed at the onset voltages are correlated with the breakdown of small portions of the main gap.

The corona extinction voltage V_{ext} was also measured by reducing the peak voltage applied at the mid-position of the plateau of the r.f. pulse. It was then found that the corona extinction voltage was slightly lower than the onset voltage. The difference arises because the onset voltage is measured by progressively increasing the r.f. peak voltage until the 'sudden' increase in luminosity is observed. If this occurs on the rising part of the r.f. pulse waveform, the corresponding r.f. peak voltage amplitude will be larger than the true corona onset voltage. Consequently the onset voltage recorded will be too high and, when the extinction voltage is recorded by reducing the r.f. voltage amplitude at the mid-position of the plateau of the pulse waveform, it will appear to be lower than the recorded onset voltage.

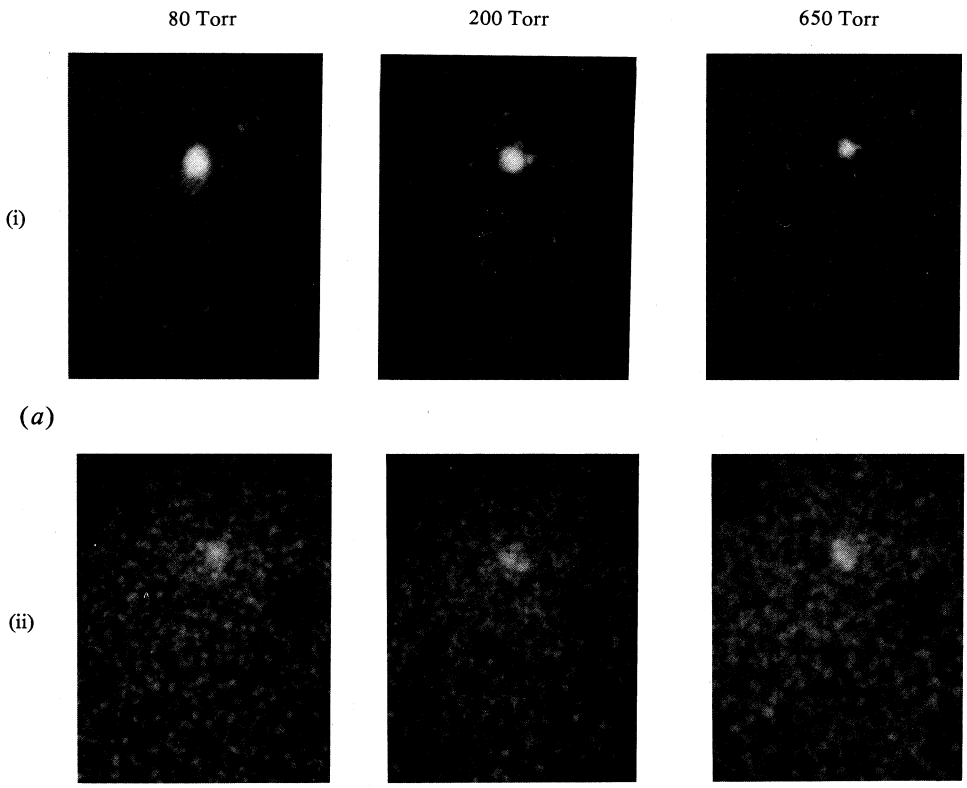

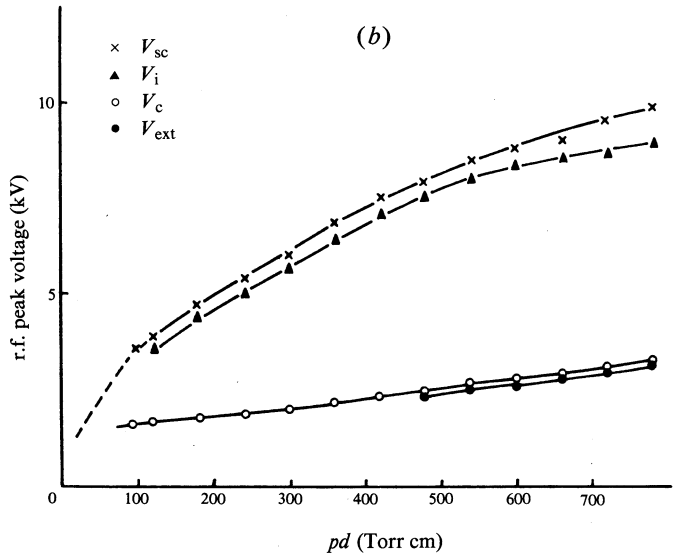

Fig. 3. (*a*) Corona images at the corona onset for various values of the gas pressure, (i) at the negative peak of the applied r.f. voltage, (ii) at the positive peak immediately prior to the corona onset. (*b*) Plots of V_{sc}, V_i, V_c and V_{ext} against pd.

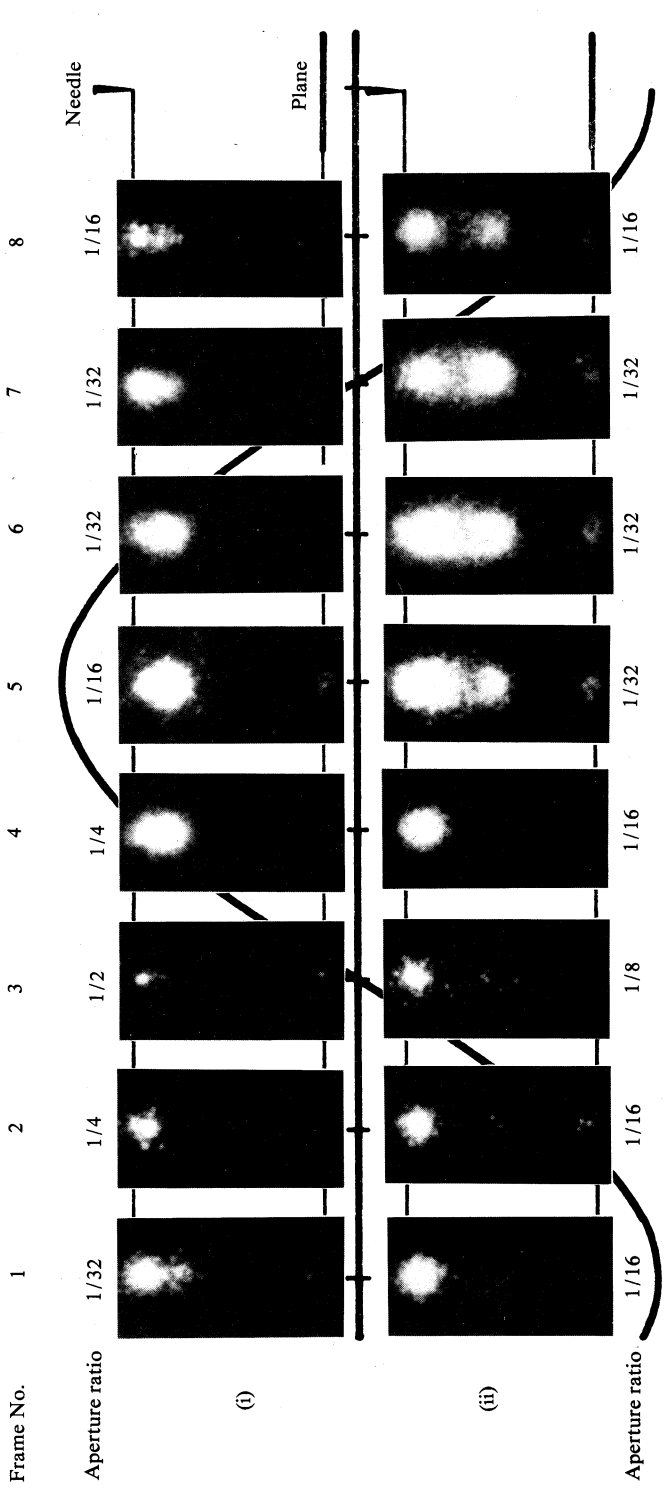

Fig. 4. Variation of the corona image at 200 Torr in N_2 for a r.f. pulse voltage $(V_p)_{max} = 3000$ V at (i) $T = 2$ μs, and an r.f. peak voltage $V_p = 2100$ V; (ii) $T = 3$ μs, $V_p = 2550$ V; (iii) $T = 5$ μs, $V_p = 3000$ V; (iv) $T = 8$ μs, $V_p = 3000$ V.

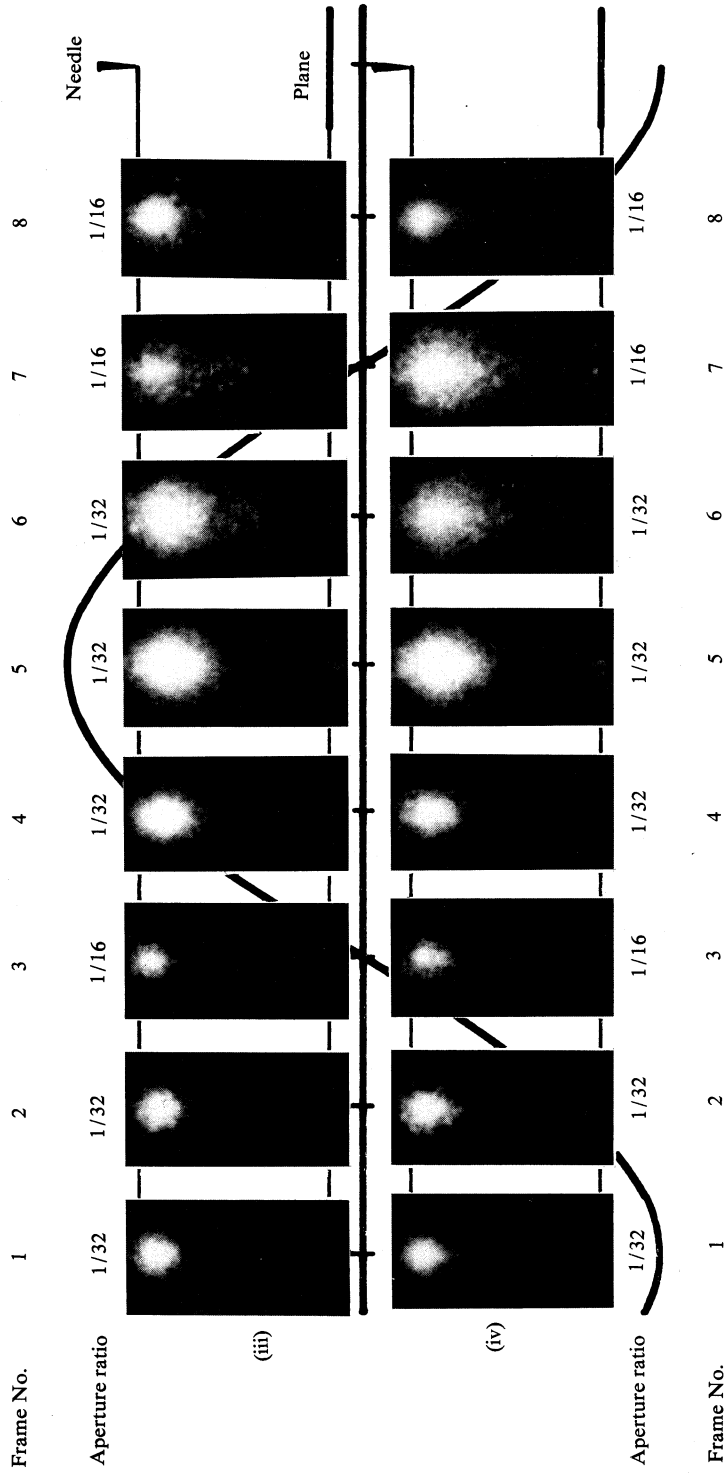

Fig. 4. *(Continued)*

With a knowledge of the extinction voltage it is possible, by careful control of the r.f. voltage amplitude, to measure the onset potential when the 'sudden' increase in the luminosity occurs close to the plateau rather than on the rising part of the pulse waveform. Under these conditions the two voltages were found to be nearly identical and this indicates that under the present conditions the corona onset is dominated by the *peak* value of the applied voltage when the corona discharge is initiated.

(b) Observations of the Corona Image at a Pressure of 200 Torr

(i) *Constant peak voltage* $(V_p)_{max} = 3000$ V. Fig. 4 shows a typical series of photographs taken at various stages of the applied r.f. voltage pulse. The peak voltage was 3000 V and the frames correspond to the phase positions 1–8 within one cycle of the r.f. voltage. It should be noted that the radiation dominating the corona images originates from the $N_2(C^3\Pi_u–B^3\Pi_g)$ transitions of N_2 molecules and that the effective lifetime associated with the excited state is comparable with the exposure time at a pressure of 200 Torr. Consequently, the radiation from the remaining excited molecules produced at an earlier phase position gives rise to radiation contributing to the corona image. At 200 Torr in nitrogen, when the effective lifetime of the $N_2(C^3\Pi_u)$ state is 9 ns, the percentage of such excited molecules remaining at the times of the succeeding exposures, 12·5 and 25 ns later, are 26% and 7% respectively. By taking this effect into account, the following significant observations can be noted:

(1) There is a distinctive spherical growth of the luminosity that completely encloses the tip of the needle electrode for almost all phase positions and stages of the applied r.f. voltage pulse. Careful examination of the recorded images reveals that at the later stage of the r.f. pulse, luminosity can be seen at the side surface of the needle near the tip.

(2) There is a distinctive polarity effect as well as hysteresis; the luminous area of the corona surrounding the needle at positive polarity is larger than that for negative polarity and the appearance of images at the two off-peak positions after the positive and before the negative peak amplitudes are different from each other.

(3) There is a distinct variation of the corona image at successive stages of the applied r.f. voltage pulse. At the negative peak position a faint luminosity extending from the tip can be observed, but only at the early stage; that is, just after the corona onset position of the r.f. pulse [frame 1, Fig. 4 (i)]. The intensity and extent of the spherical luminosity around the tip of the needle increases at the later stages. At the positive peak position, the variation of the image with successive stages can be classified into three types: a spherically localized luminosity around the tip of the needle [Type A, e.g. Fig. 4 (i), $T = 2$ μs, frame 5], which is extended towards the plane electrode in the shape of an ellipsoid [Type B, e.g. Fig. 4 (ii), $T = 3$ μs, frame 5] and is then diffused to a pear shape [Type C, e.g. Fig. 4 (iii) and (iv), $T = 5$ and 8 μs, frame 5].

(ii) *Variation with* $(V_p)_{max}$. The corona images observed with the peak values of r.f. voltage pulse of 2550 and 3600 V are basically the same as the images observed at 3000 V. However, Type B and C images appear at earlier stages with increasing applied peak voltage. The various measured time delays T, from the start of the r.f. pulse to the appearance of the particular image type, are summarized in Table 1.

Table 1. Time delays T for the appearance of various types of images

$(V_p)_{max}$ (kV)	Corona onset		Type A		Type B		Type C	
	τ (μs)	V_c (kV)	T (μs)	V (kV)	T (μs)	V (kV)	T (μs)	V (kV)
2·55	1·5	1·95	1·5–2·1	1·95–2·4	2·1–5·5	2·4–2·5	5·5–10	2·55
3·00	1·2	2·05	1·2–1·5	2·05–2·40	1·5–3·4	2·4–3·0	3·4–10	3·0
3·60	1·0	2·10	1·0–1·4	2·10–2·55	1·4–2·4	2·55–3·3	2·4–10	3·3–3·6

(c) Factors Influencing Gap Luminosity

A general appreciation of the mechanism responsible for, and the parameters influencing the growth and decay of, luminosity in the needle-to-plane gap requires consideration of the electric fields in the gap.

(i) *Space charge free electric fields.* For the particular case of a needle-shape corresponding to a hyperboloid of revolution, the electric field, in the absence of space charge effects, has been calculated previously (Eyring *et al.* 1928; Lama and Gallo 1974; Fujita 1980). With spheroidal coordinates the field distribution is represented by

$$E_\theta = -V_a/a(\sinh^2\eta + \sin^2\theta)^{\frac{1}{2}} \sin\theta \log(\tan\tfrac{1}{2}\theta_0), \tag{5}$$

where V_a is the voltage applied to the needle electrode and $\theta = \theta_0$ on the needle surface. The maximum amplitude of an electron travelling in this field during one cycle of the r.f. field is calculated by solving the equation

$$a\sinh\eta \sin\theta \, \mathrm{d}\theta/\mathrm{d}t = W_e = \mu E, \tag{6}$$

where μ is the electron mobility and W_e is the electron drift velocity. Calculation shows that electrons released from the needle electrode are confined to a region within about 2 mm of the needle electrode surface as shown in Fig. 5*a*. In this high field region the electron density produced by ionization amplification can be sustained by the photon-induced (γ_p) secondary effect and this produces sufficient numbers of excited molecules to cause the spherical luminosity observable around the needle tip and which extends thinly along the side of the needle surface. In spheroidal coordinates, the secondary electron density $N\gamma_p$ arising from the γ_p effect at the position $(\eta_0, \theta_0, \phi_0)$ on the needle electrode surface is

$$N\gamma_p(\eta_0, \theta_0, \phi_0, t) = \frac{\Gamma_p}{\tau_0 \, W_e(\eta_0, \theta_0, \phi_0, t)} \iiint g(\eta_0, \theta_0, \phi_0; \eta, \theta, \phi) \, n_{ex}(\eta, \theta, \phi) \times a^3(\sinh^2\eta + \sin^2\theta)\sinh\eta \sin\theta \, \mathrm{d}\eta \, \mathrm{d}\theta \, \mathrm{d}\phi. \tag{7}$$

Here $n_{ex}(\eta, \theta, \phi)$, Γ_p and τ_0 are respectively the density of excited molecules at the position (η, θ, ϕ), the photo-electron emission efficiency of the needle surface and the lifetime of the excited state; g is a geometrical factor given by

$$g = \tfrac{1}{4}\pi^{-1} \frac{\boldsymbol{n}.\boldsymbol{R}}{|\boldsymbol{R}|^3}, \tag{8}$$

where $\boldsymbol{n}$ is the unit normal vector at $(\eta_0, \theta_0, \phi_0)$ on the needle surface and $\boldsymbol{R}$ is

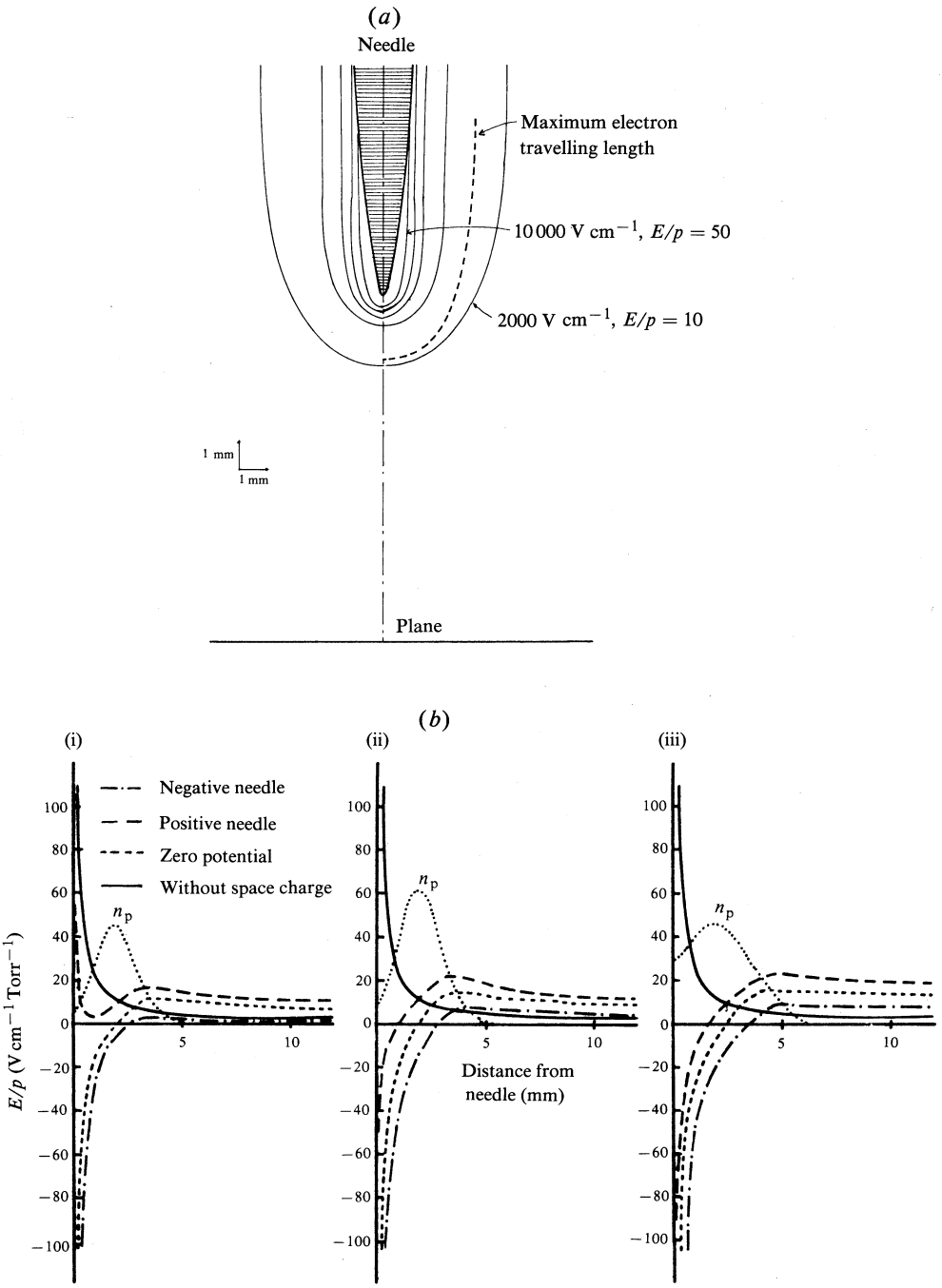

Fig. 5. (*a*) Electric field strength contour in the range of E/p values between 10 and 50 V cm^{-1} Torr^{-1} (E/N values between 28 and 141 Td, where 1 Td = 10^{-17} V cm^2; N = gas number density) at V_p = 3000 V and 200 Torr. (*b*) Variation of the electric field due to the positive space charge in N_2 at 200 Torr for peak values of the positive charge distribution n_p (dotted curve) of (i) $1{\cdot}5\times10^{10}$ cm^{-3}, (ii) 2×10^{10} cm^{-3} and (iii) $1{\cdot}5\times10^{10}$ cm^{-3} but with a wider distribution.

the distance between a photon source (η, θ, ϕ) and the position $(\eta_0, \theta_0, \phi_0)$. It is the geometrical factor which prevents the growth of the luminosity along the needle surface to positions far away from the needle tip. This is because g decreases rapidly with increasing η_0, the distance from the tip along the needle surface.

(ii) *Space charge effects.* In order to understand the extension of the luminosity towards the plane electrode, space charge fields must be taken into account. For this purpose Poisson's equation in spheroidal coordinates must be solved:

$$\nabla . E = \frac{1}{h_1 h_2 h_3}\left(\frac{\partial}{\partial\eta}(h_2 h_3 E_\eta) + \frac{\partial}{\partial\theta}(h_3 h_1 E_\theta) + \frac{\partial}{\partial\phi}(h_1 h_2 E_\phi)\right) = \frac{e\rho(\eta, \theta, \phi)}{\epsilon_0}, \quad (9)$$

where $h_1 = h_2 = a(\sinh^2\eta + \sin^2\theta)^{\frac{1}{2}}$, $h_3 = a\sinh\eta\sin\theta$, ρ is the charge density and ϵ_0 is the permittivity of free space.

Equation (9) reduces to a one-dimensional equation which has an exact solution if E_η and E_ϕ can be ignored. This is a reasonable approximation to adopt considering the symmetry of the electrode configuration about the ϕ axis and given the symmetry of the expanded corona image about the direction of η. In such a case, E_θ for the negative needle electrode is given by

$$\begin{aligned} E_\theta = {} & \frac{V_0 \sin\omega_0 t}{a(\sinh^2\eta + \sin^2\theta)^{\frac{1}{2}}\sin\theta\log(\tan\frac{1}{2}\theta_0)} \\ & - \frac{1}{(\sinh^2\eta + \sin^2\theta)^{\frac{1}{2}}\sin\theta\log(\tan\frac{1}{2}\theta_0)} \\ & \times \int_{\theta_0}^{\pi} \log(\tan\tfrac{1}{2}\theta)\frac{ae\rho}{\epsilon_0}(\sinh^2\eta + \sin^2\theta)\sin\theta\,\mathrm{d}\theta \\ & + \frac{1}{(\sinh^2\eta + \sin^2\theta)^{\frac{1}{2}}\sin\theta}\int_{\theta_0}^{\theta}\frac{ae\rho}{\epsilon_0}(\sinh^2\eta + \sin^2\theta')\sin\theta'\,\mathrm{d}\theta', \end{aligned} \quad (10)$$

where V_0 and ω_0 are the peak voltage and angular frequency of the applied r.f. voltage. If the positive charge distribution $\rho(\theta)$ is known in the high field region in front of the needle electrode, then E_θ can be calculated numerically by the use of a computer.

(iii) *Effect of magnitude and distribution of net positive charge densities.* Fig. 5*b* shows variations of the electric field in the gap space for three different assumptions about the space charge densities and distribution. In each case the electric field has been calculated for the needle electrode at either negative, positive or zero potential and also included is the electric field distribution in the absence of any space charge.

In the neighbourhood of the needle the electric field is enhanced when the polarity of the needle is negative and decreased when it is positive. This explains why the luminosity is localized around the needle tip for negative polarity. By contrast the space charge field increases the electric field in a region separated from the needle point in the case of positive polarity and results in increased luminosity further away from the needle point in these cases.

With an increase in the magnitude of the space charge and a more extensive distribution, the peak of the electric field moves towards the plane electrode and the field between mid-gap and the plane becomes nearly uniform and high enough to create high populations of excited states. This explains not only the appearance of mid-gap luminosity but also its extension towards the plane electrode.

For zero potential at the needle electrode the influence of the space charge field remains and creates a field sufficiently large at the needle point to produce luminosity. For the higher assumed space charge densities a similar situation is created in mid-gap. This explains the observations of luminosity at both the needle point and in mid-gap shown clearly in frame 7 of Fig. 4 (ii).

It remains now to understand the causes of the progressive changes of the corona image from those of Type A to those of Type C. This can be explained in terms of variations in the space charge distribution due to the ionization process and drift motion of the charged particles (Sato and Haydon 1984*b*). The increase in the magnitude of the assumed space charge distribution from Fig. 5*b* (i) to (ii) due to ionization is followed by the more diffuse distribution assumed in Fig. 5*b* (iii) which can be attributed to the consequences of the ions remaining quasi-stationary during a single cycle of the r.f. voltage and so reducing and extending the space charge distribution. This comes about essentially by drift motion in the space charge field itself.

Such effects clearly need to be examined with the help of appropriate computer simulation techniques by using the continuity equation together with Poisson's equation to achieve a detailed understanding of these phenomena and this is currently in progress (Sato and Tagashira 1985).

(d) Multi-exposure Observations of the Corona Image by Two-stage MCP Image Intensification

In this subsection corona images at pressures of 200 and 80 Torr are compared. Fig. 6*a* (i) and (ii) shows the corona images at a pressure of 200 Torr with time delays of 3 and 5 μs from the start of the 3000 V peak r.f. pulse, which corresponds with Fig. 4 (ii) and (iii) respectively. It can be seen that the appearance of images taken by the two-stage intensifier photographs are basically the same as those taken by the three-stage intensifier. However, since the deterioration of the image caused by the MII is now avoidable, more clearly focused photographs can be obtained. Such photographs show clearly, for the off-peak and zero potential phase positions following the positive peak polarity (frames 6 and 7 of Fig. 6*a*), the existence of a thin bright emission in the neighbourhood of the needle tip surrounded by a fainter and more diffuse luminosity. These observations can be explained by the high field caused by space charge in the neighbourhood of the needle tip, as discussed above.

Fig. 6*b* shows a typical diagram of the spatial intensity variation of the corona image obtained by the OMA system. This quantitative data can be used for comparison with the data obtained by a computer simulation.

The corresponding information for a pressure of 80 Torr is given in Fig. 7. At 80 Torr the corona images are affected by the persistence of radiation from the excited molecules because the effective lifetime of the excited state is then about 20 ns and the percentage of excited molecules remaining at the time of the succeeding exposure is about 50%. In spite of this, the polarity effect, hysteresis and progressive change

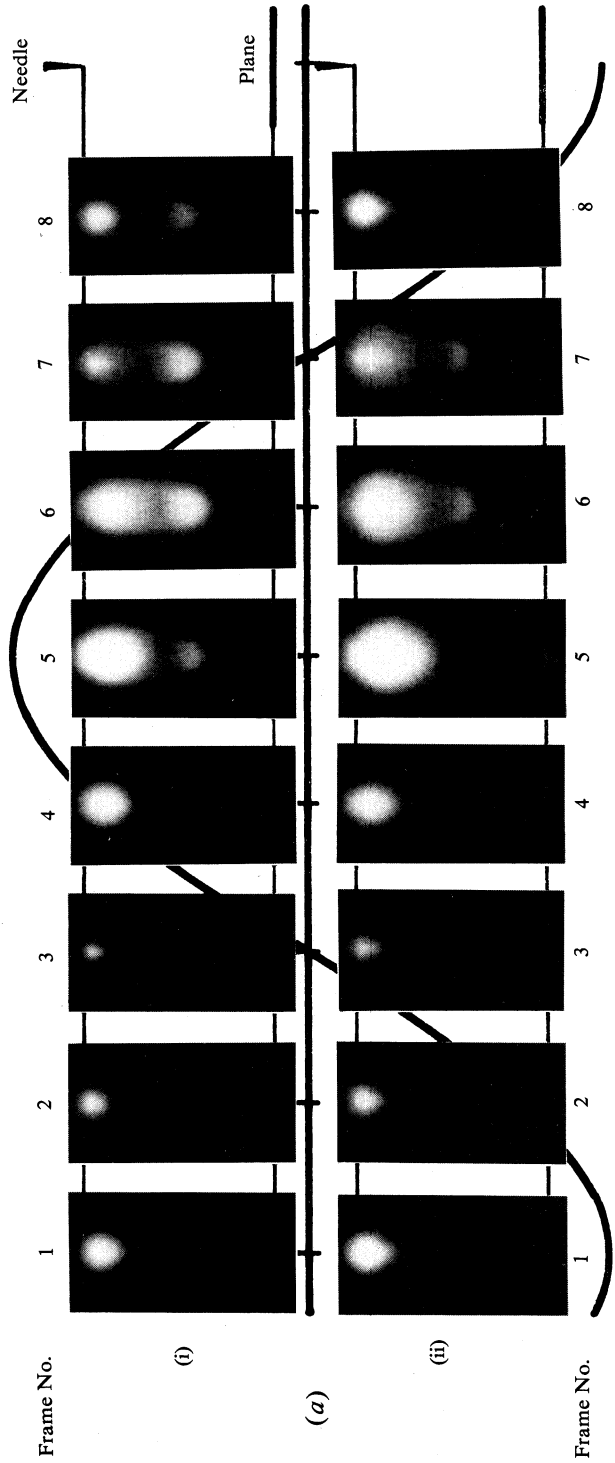

Fig. 6. (*a*) Variation of the corona image at 200 Torr taken with two-stage MCP image intensification and multi-exposures (50 times) at
(i) $T = 3\ \mu s$, $V_p = 2550$ V;
(ii) $T = 5\ \mu s$, $V_p = 3000$ V.
(*b*) Intensity variation of the corona image at 200 Torr at the positive peak [frame 5 of (*a*) (i)].

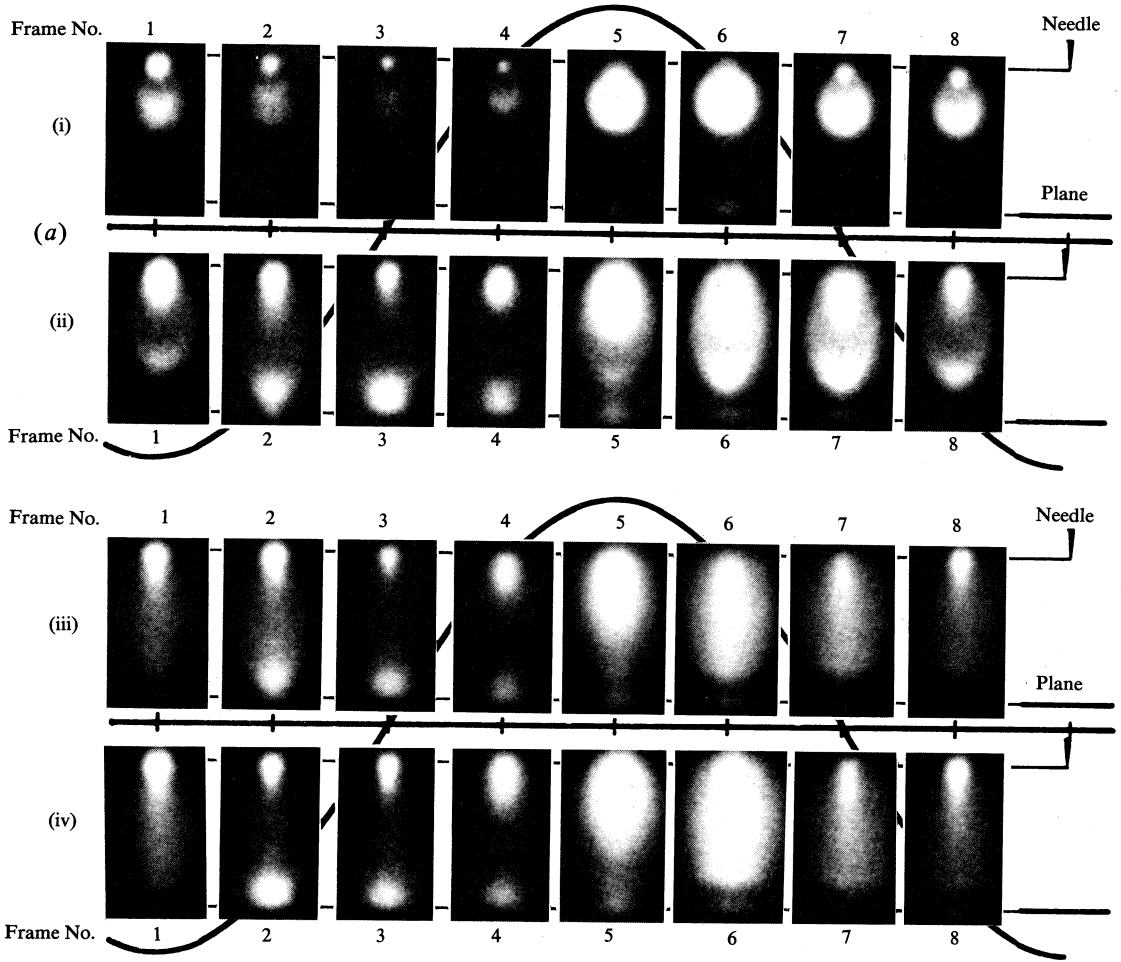

Fig. 7. (*a*) Variation of the corona image at 80 Torr taken with two-stage MCP image intensification and multi-exposures (25 times) at (i) $T = 2\ \mu s$, $V_p = 1650$ V; (ii) $T = 3\ \mu s$, $V_p = 1950$ V; (iii) $T = 5\ \mu s$, $V_p = 2100$ V; (iv) $T = 8\ \mu s$, $V_p = 2100$ V. (*b*) Intensity variation of the corona image at 80 Torr at the off-peak phase position after the positive peak [frame 6 of (*a*) (ii)].

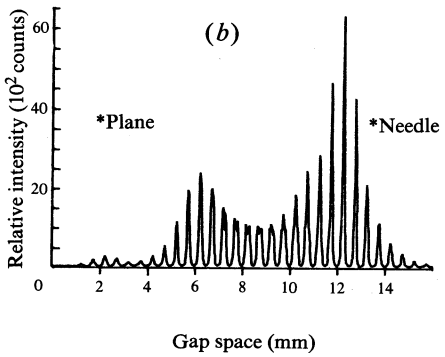

of images from Type A to C can still be identified. In comparison with the corona images observed at 200 Torr, those observed at 80 Torr are more expanded at the early stages and more extended at the later stages. Furthermore, localized luminosity appears in the neighbourhood of the plane electrode at both the off-peak and zero positions after the negative peak voltage (frames 2 and 3 of Fig. 7*a*).

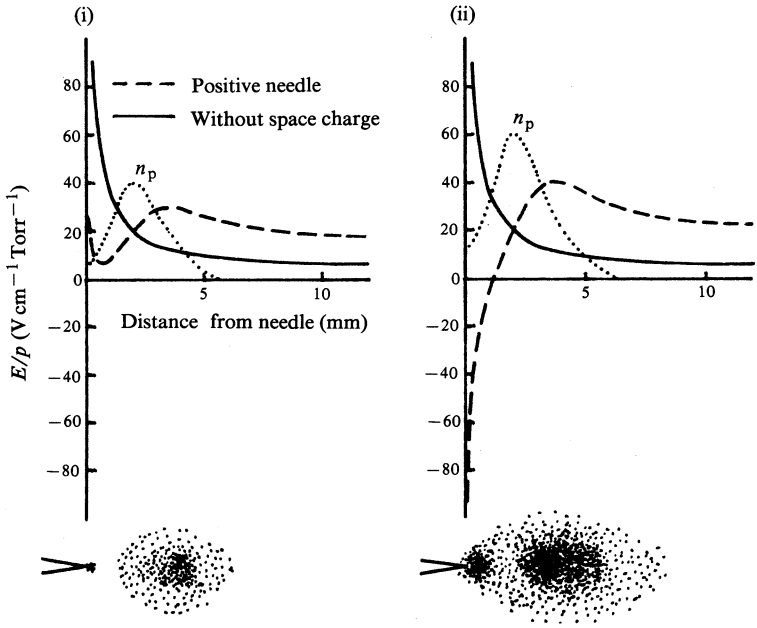

Fig. 8. Variation of the electric field due to various positive space charge densities at $p = 80$ Torr in N_2 and schematic representation of anticipated corona images based on electric field variations for n_p values of (i) $1{\cdot}0\times10^{10}$ cm^{-3} and (ii) $1{\cdot}5\times10^{10}$ cm^{-3}.

(e) Examination of the Space Charge Influences at Lower Gas Pressures

The more complex phenomena observed at low pressures require a more detailed examination of the consequence of the influence of space charge fields. In particular, it is essential to appreciate the sensitivity that emerges under these low pressure conditions to the assumptions made about the magnitude and spatial distribution of the positive ion density. For the case of N_2 at 200 Torr the positive ion densities were assumed to be either $1{\cdot}5$ or $2{\cdot}0\times10^{10}$ cm^{-3} and the effect of adjusting the spatial distribution for a density of $1{\cdot}5\times10^{10}$ cm^{-3} was examined separately. The space charge influences created very large negative electric fields in the neighbourhood of the needle point for all phase positions except for a narrow distribution at $1{\cdot}5\times10^{10}$ cm^{-3} (Fig. 5*b*). The extent of the luminosity about the needle point correlated with these calculated variations of the negative electric field into the mid-gap region. By contrast the fine structure of the luminosity observed at 80 Torr cannot be explained in the same way.

The difficulties may be appreciated by examining the variation of the electric fields caused by positive space charge under these lower pressure conditions. Fig. 8 shows the results of calculations for two different assumed values of the positive ion density, (i) $1{\cdot}0\times10^{10}$ cm^{-3} and (ii) $1{\cdot}5\times10^{10}$ cm^{-3}. The important features are:

(1) For large values of the positive ion density in (ii) the electric field for a positive needle potential assumes large negative field gradients close to the needle tip. In other words, the space charge terms in equation (10) dominate the character of the space charge distorted electric fields.

(2) For a lower value of the positive ion density in (i) these space charge terms do not exert an overriding influence and a large positive electric field exists at the needle tip. The nature of the competition between the space charge free electric fields and those created by the space charges themselves results in a minimum value at some distance in front of the needle point. The strength of these positive electric fields and their extent towards the mid-gap region are very sensitive to both the assumed values of the positive ion density and its distribution.

(3) As the positive ion density is reduced and distributed further towards the mid-gap region the influence of the space charge terms dominates and a negative electric field becomes established in the neighbourhood of the needle point.

(4) At regions close to the plane electrode there is always an increase in the magnitude of the substantially uniform electric field with an increase in the assumed value of the positive ion density. The appearance of luminosity on the region of the plane electrode is therefore significant in helping to remove ambiguities that may arise because of the complex behaviour that is possible near the needle point itself.

With an appreciation of these space charge influences it is now possible to anticipate the structure of the luminosity that might appear whenever low values of positive ion density appear. This is most likely for the very early stages of the development of corona at all pressures. Furthermore, it might be expected that as the gas pressure is increased from low to high pressures then the luminosity surrounding the needle point might diminish in spatial extent and appear to collapse into the needle, to re-emerge as a more extensive luminous region when the positive ion densities have built up to values large enough to ensure very large negative electric fields at the needle point at all stages. Schematically, these possible variations in the luminous phenomena are shown in Fig. 8 (i) for a positive needle electrode.

(f) Observations of Corona Images at Pressures of 80 and 650 Torr

As outlined in Section 3*d*, the persistence of radiation from excited molecules complicates the interpretation of the detailed structure of the luminosity at 80 Torr. Nevertheless some of the features to be anticipated in view of the analyses given in Section 3*e* can be identified, since only 50% of the observed luminosity can be attributed to the persistence phenomenon. For example, frames 7 and 8 of Fig. 7*a* (i) show a limited bright spot close to the needle point which, at the later stage $T = 3$ μs (ii), becomes a more extensive region of luminosity following an increase in positive ion density and a change to a large negative electric field at the needle point. The increased luminosity close to the plane electrode confirms that an increase in the positive ion density has occurred. Furthermore, the bright spots close to the needle point for negative peak potential are larger than those for the positive peak, as would be expected when the negative electric field variation has been established.

At higher pressures of 650 Torr, the luminosities observed (Fig. 9*a*) are less extensive and less expanded than those at 80 Torr. Nevertheless the variations of the

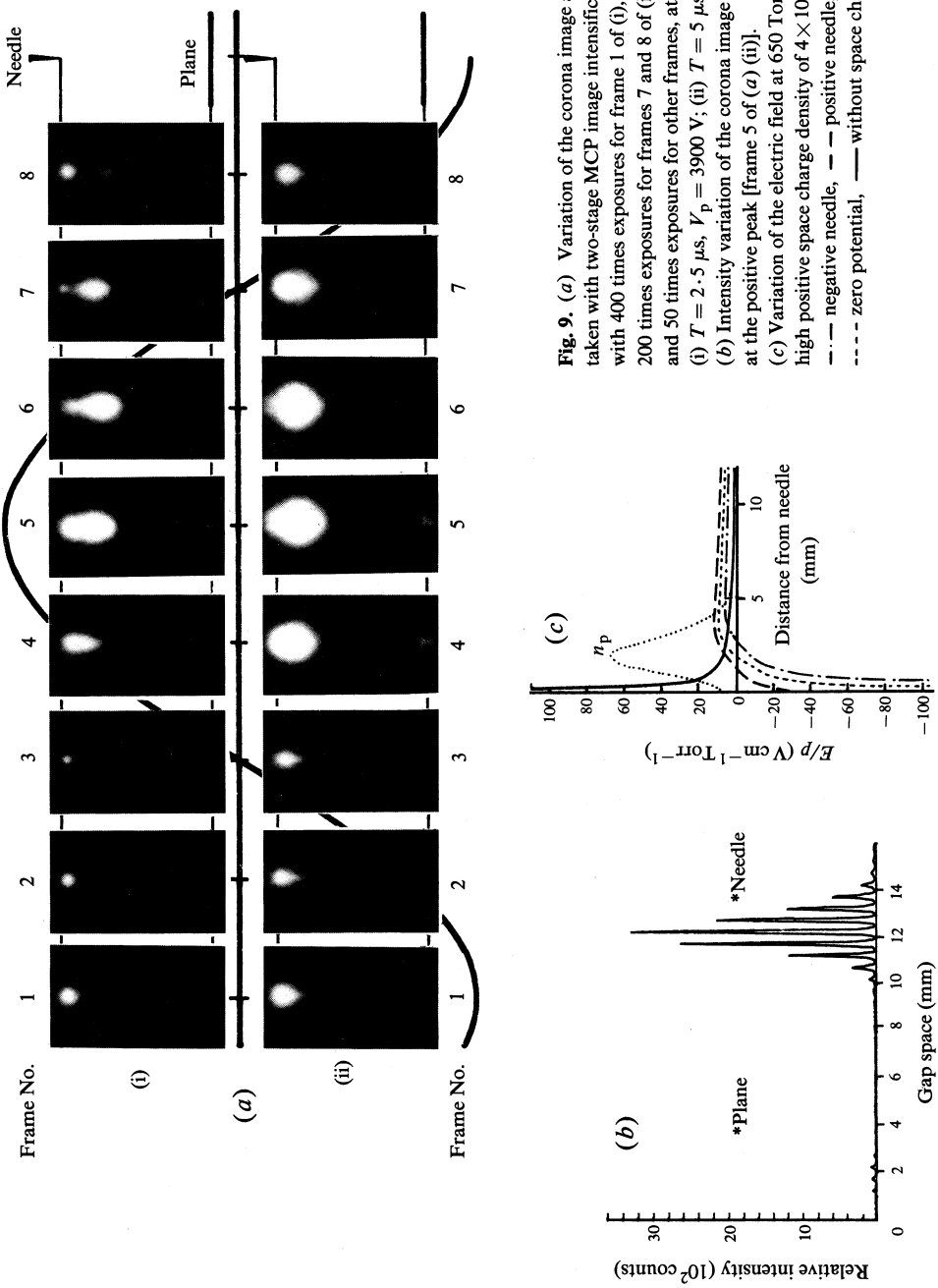

Fig. 9. (*a*) Variation of the corona image at 650 Torr taken with two-stage MCP image intensification with 400 times exposures for frame 1 of (i), 200 times exposures for frames 7 and 8 of (i) and 50 times exposures for other frames, at (i) $T = 2{\cdot}5$ μs, $V_p = 3900$ V; (ii) $T = 5$ μs, $V_p = 6000$ V. (*b*) Intensity variation of the corona image at 650 Torr at the positive peak [frame 5 of (*a*) (ii)]. (*c*) Variation of the electric field at 650 Torr due to high positive space charge density of 4×10^{10} cm^{-3}; -·— negative needle, — — positive needle, - - - - zero potential, —— without space charge.

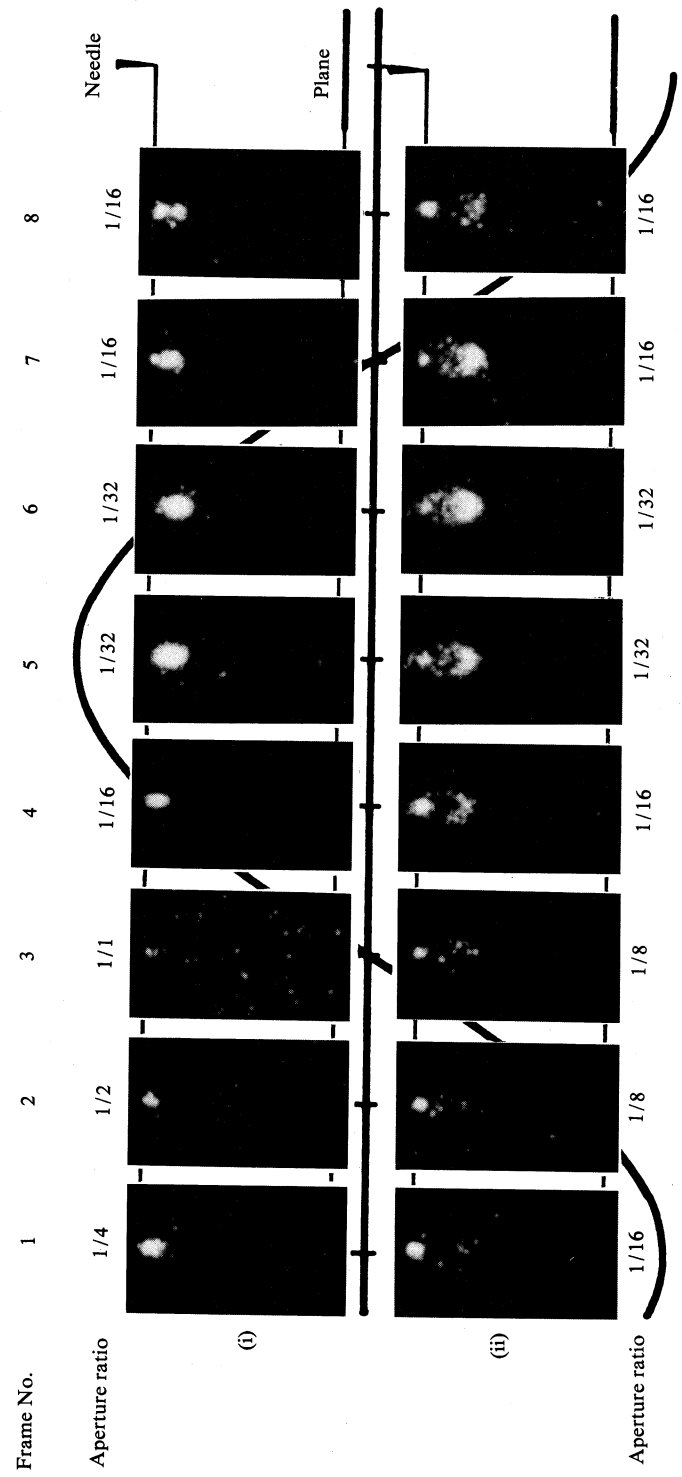

Fig. 10. Variation of the corona image at 200 Torr taken with the u.v. filter at (i) $T = 1{\cdot}1\ \mu s$, $V_p = 2100$ V; (ii) $T = 1{\cdot}8\ \mu s$, $V_p = 2550$ V; (iii) $T = 5\ \mu s$, $V_p = 3000$ V; (iv) $T = 8\ \mu s$, $V_p = 3000$ V.

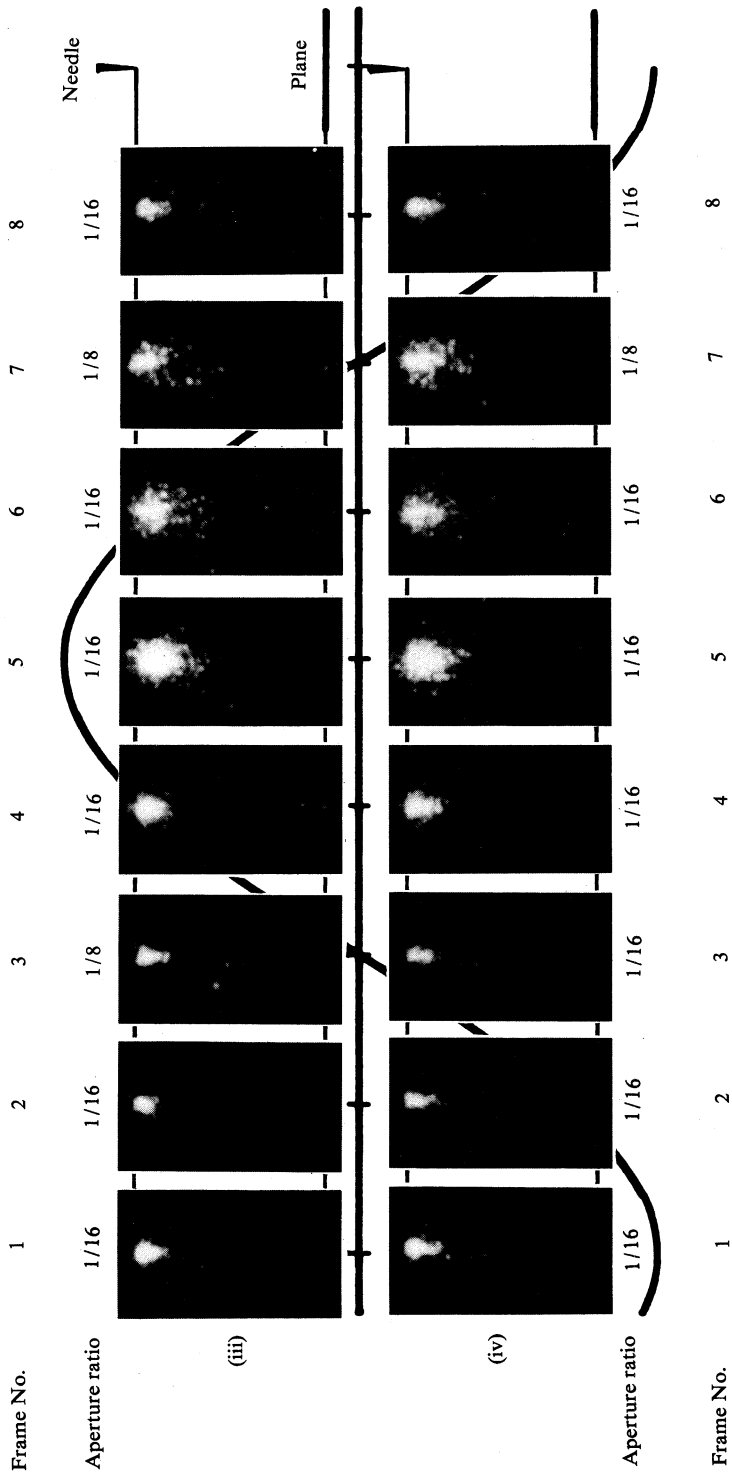

Fig. 10. *(Continued)*

corona images with change of phase position, different stage and variation of peak applied r.f. voltage are basically the same. The intensity variations corresponding to the particular luminosity observed at the positive peak position are shown in Fig. 9*b*, whilst Fig. 9*c* shows the calculated variation of the electric field caused by the space charge effect. It should be noted for this case that the assumed positive ion density, 4×10^{10} cm^{-3}, is too high for any large positive electric field to remain in the neighbourhood of the needle electrode. Furthermore, the negative electric field produced by the space charge effect is confined to the region very close to the needle tip. This explains the appearance of the concentrated luminosity around the tip of the needle electrode.

(g) Effect of u.v. Filtering

With the Kodak 2C u.v. filter (see Fig. 2) photographs of the corona images were recorded (Fig. 10) at a pressure of 200 Torr at the various stages of the applied r.f. pulse shown in Fig. 4. Only the core of the corona discharge is observed in this case, the expanded and extended luminosities having been eliminated by the filtering. This demonstrates that the corona discharge has some structure caused by a radially dependent electron energy distribution as well as a distribution varying along the direction of the symmetry axis of the electrodes. The effect of the filtering is to remove the high intensity emission lines of the second positive system but to retain the radiation from the (0, 0) transition of the first negative system of N_2^+ and the weak emission lines due to transitions between higher vibrational levels of the first and second positive systems of neutral nitrogen molecules. Interpretation of these observations requires further analysis based on a computer simulation of the experiment which is now in progress.

4. Conclusions

The use of highly time-resolved image intensifier and spectroscopic techniques to examine corona onset and subsequent plasma growth in the space between a hyperboloidal needle and plane electrode have confirmed the general features of r.f. plasma growth observed with toroid–plane geometry (Sato and Haydon 1984*a*, 1984*b*). Furthermore, the use of electrode geometry amenable to mathematical analysis has provided clarification of the underlying causes of the significant features of the ionization growth under r.f. conditions. In particular:

(1) The combined effects of the extended high field region along the needle surface, the limited amplitude of the electron motion during one cycle of the r.f. field and the geometrical factors influencing the secondary ionization effects at the needle surface account for the distinctive spherical growth of the luminosity that completely encloses the needle tip at almost all phase positions and stages of the r.f. voltage pulse.

(2) The calculated space charge field variations show that it is the formation and re-distribution of the positive ion space charge in the gap that is essentially responsible for the observed polarity and hysteresis effects as well as the progressive changes from spherically localized to extended ellipsoidal and finally to diffused pear-shaped corona images.

(3) The observed time intervals required for the progressive changes of these corona images indicate that the time constant associated with the space charge

accumulation and re-distribution processes is of the order of μs and that the equilibrium balance between the space charge accumulation and loss processes is achieved at earlier times with increasing applied peak voltage.

(4) Furthermore, the structure of the corona discharge revealed by the use of a u.v. filter indicates the existence of both a radially dependent electron energy distribution as well as an axially varying distribution. Further experiments with a combination of filters should provide new information on these variations.

(5) Finally, it should be noted that there are some features of the corona image such as hysteresis which cannot be explained by the sole influence of positive space charges. In order to understand such phenomena further computer-aided analyses are required which should take into account the effect of electron motion and electron density distribution on the variation of the corona images.

Acknowledgments

The authors have greatly appreciated the continuing financial support received from the Electrical Research Board for this particular project, which forms part of a wider program of investigations into basic electrical discharge mechanisms which the Board also supports.

They also wish to acknowledge the support for equipment purchases made available by Telecom Australia and the Australian Institute of Nuclear Science and Engineering during the course of the investigation.

References

Cook, D. C., and Haydon, S. C. (1984). *IEEE Proc.* A **131**, 153–8.

Dossing, S., Lobert, O., Bondarenko, E. J., Haydon, S. C., and Plumb, I. C. (1978). *Aust. Telecommun. Res.* **10**, 3–23.

Eyring, C. F., Mackeown, S. S., and Millikan, H. A. (1928). *Phys. Rev.* **31**, 900–9.

Fujita, H. (1980). *IEEE Jpn* A **100**, 323–30.

Haydon, S. C., and Plumb, I. C. (1978). *Aust. Telecommun. Res.* **10**, 24–8.

Lama, W. L., and Gallo, C. F. (1974). *J. Appl. Phys.* **45**, 103–10.

Plumb, I. C., Cook, D. C., and Haydon, S. C. (1984). *IEEE Proc.* A **131**, 145–52.

Sato, N., and Haydon, S. C. (1984*a*). *J. Phys.* D **17**, 2009–21.

Sato, N., and Haydon, S. C. (1984*b*). *J. Phys.* D **17**, 2023–36.

Sato, N., and Tagashira, H. (1985). Study on the simulation of the r.f. discharge in N_2. Bulletin of Faculty of Engineering, Hokkaido University, Vol. 126, pp. 21–34.

Manuscript received 19 August, accepted 20 December 1985